Journal of
Materials Chemistry A

PAPER

View Article Online
View Journal | View Issue

Cite this: *J. Mater. Chem. A*, 2016, **4**, 2670

# Hydrogen treated anatase $TiO_2$: a new experimental approach and further insights from theory†

Manan Mehta,[af] Nisha Kodan,[b] Sandeeep Kumar,[c] Akshey Kaushal,[b]
Leonhard Mayrhofer,[de] Michael Walter,[de] Michael Moseler,[de] Avishek Dey,[f]
Satheesh Krishnamurthy,[f] Suddhasatwa Basu*[a] and Aadesh P. Singh*[b]

Hydrogenated $TiO_2$ (H:$TiO_2$) is intensively investigated due to its improvement in solar absorption, but there are major issues related to its structural, optical and electronic properties and therefore an easily compatible method of preparation is much needed. In order to clarify this issue we studied $TiO_2$ nanocrystals under the partial pressure of hydrogen to modify the structural, optical and electrical properties and to significantly improve the photocatalytic and photoelectrochemical performance. The hydrogen treated $TiO_2$ nanocrystals contained paramagnetic $Ti^{3+}$ centers and exhibited a higher visible light absorption cross-section as was confirmed by electron paramagnetic resonance diffuse reflectance spectra measurements and X-ray photoelectron spectroscopy. The hydrogen annealed samples showed a noticeable improvement in photocatalytic activity under visible light ($\lambda > 380$ nm) which was demonstrated by the degradation of methylene blue dye and an improved photoelectrochemical response in terms of high photocurrent density. *Ab initio* simulations of $TiO_2$ were performed in order to elucidate the conditions under which localized $Ti^{3+}$ centres rather than delocalized shallow donor states are created upon the reduction of $TiO_2$. Randomly distributed oxygen vacancies lead to localized deep donor states while the occupation of the oxygen vacancies by atomic hydrogen favours the delocalized shallow donor solution. Furthermore, it was found that localization is stabilized at high defect concentrations and destabilized under external pressures. In those cases where localized $Ti^{3+}$ states are present, the DFT simulations showed a considerable enhancement of the visible light absorption as well as a pronounced broadening of the localized $Ti^{3+}$ energy levels with increasing defect concentration.

Received 8th September 2015
Accepted 15th January 2016

DOI: 10.1039/c5ta07133j

www.rsc.org/MaterialsA

## 1. Introduction

Nanosized titanium dioxide ($TiO_2$) in the anatase phase has been extensively used in solar driven photocatalytic processes for hydrogen production and water decontamination.[1–3] However, its large bandgap (∼3.2 eV) requires light below 388 nm to create an electron–hole pair and limits the overall efficiency. Therefore, in order to increase absorption of $TiO_2$ for natural solar radiation, a variety of techniques have been reported such as metal ion doping,[4,5] anion doping,[6,7] noble metal loading,[8,9] addition of electron donors,[10] metal ion-implantation[11] and self-doping that produce $Ti^{3+}$ species[12] *etc.* At present, anion-doped $TiO_2$ (especially nitrogen doping in $TiO_2$) exhibits the greatest optical response to the visible region, due to its modified electronic transition from the dopant 2p orbitals to the Ti3d orbitals which is responsible for the visible light absorption. However, N-doped $TiO_2$ still has no sufficient absorption in the visible region.[6]

Over the past few years hydrogen induced modification in metal oxide semiconductors has been of substantial interest due to their higher photocatalytic performance. Hydrogen treatment techniques play a key role in tailoring the optical and electronic properties of metal oxide thin films and nanoparticles. Various hydrogen treatment processes such as high pressure hydrogen annealing,[13,14] electrochemical hydrogenation[15,16] and hydrogen plasma[17,18] for making black metal oxide nanoparticles and thin films have been used to modify the optical, electrical and photocatalytic properties. Different

---

[a] *Department of Chemical Engineering, Indian Institute of Technology, HauzKhas, New Delhi-110016, India. E-mail: sbasu@iitd.ac.in; Fax: +91 11 26581120; Tel: +91 11 26591035*

[b] *Department of Physics, Indian Institute of Technology, Hauz Khas, New Delhi-110016, India. E-mail: aadshp1982@gmail.com*

[c] *Department of Chemistry, Indian Institute of Technology, Hauz Khas, New Delhi-110016, India*

[d] *Fraunhofer IWM, Wöhlerstr. 11, D-79108 Freiburg, Germany*

[e] *University of Freiburg, FMF - Freiburg Materials Research Center, Stefan-Meier-Str. 21, D-79104 Freiburg, Germany*

[f] *Department of Engineering and Innovation, The Open University, Milton Keynes, MK7 6AA, UK*

† Electronic supplementary information (ESI) available. See DOI: 10.1039/c5ta07133j

hydrogen treatment processes lead to different properties of the hydrogen modified $TiO_2$ materials. Chen *et al.* reported that $TiO_2$ nanocrystals treated in a hydrogen atmosphere under a 20 bar $H_2$ atmosphere for 5 days showed a colour change to black with a reduction in the bandgap energy up to ~1.54 eV.[13,14] They have reported that the change in colour is due to the surface disorder of $TiO_2$ nanoparticles. The colour change in the metal oxide due to hydrogen depends upon the hydrogen treatment temperature, the partial pressure and also on the nature of hydrogen species, while in the work of Chen *et al.*[13] the narrowing of the band gap could be traced back to the surface disorder without the formation of $Ti^{3+}$ centres; other studies[12] found strong evidence that lattice defects such as oxygen vacancies can form localized $Ti^{3+}$ centres within the $TiO_2$ bandgap. Moreover, in the work of Wang *et al.*[17] hydrogen doping created a high density of delocalized Ti3d electrons leading to improved charge transport properties.

Different hydrogen treatment processes lead to different properties of the hydrogen modified $TiO_2$ materials. Hydrogen annealing of $TiO_2$ under high pressure did not show any detectable $Ti^{3+}$ states, but, produces disordered surface layers over the crystalline $TiO_2$ particles forming a core–shell structure.[13] Reduction of $TiO_2$ particles in a $H_2$ atmosphere at 500 °C shows the formation of a crystalline core/amorphous shell ($TiO_2@TiO_{2-x}H_x$) structure with about 83% absorption of solar light.[17] Hydrogen plasma treatment in $TiO_2$ nanotubes has been observed to result in simultaneously incorporated $Ti^{3+}$ and –OH groups.[19] Hydrogen plasma treated ALD grown $TiO_2$ thin films also show the formation of $Ti^{3+}$ states.[20] Electrochemical $H^+$ doping in $TiO_2$ films also exhibits the presence of $Ti^{3+}$ and –OH that may lead to additional electronic states in the band gap and shift light absorption to the visible region.[18] Different hydroxyl groups present on $TiO_2$ surfaces are supposed to participate in electron trapping in $TiO_2$ and other oxides.[21] Reduction of $TiO_2$ and –OH group formation has also been reported in theoretical hybrid density functional (B3LYP) based studies on hydrogen doping in $TiO_2$.[19,22]

Although, encouraging results on hydrogen treated $TiO_2$ have been obtained,[13,14] a detailed understanding of the role of hydrogen species (*e.g.* atomic, molecular or ionic hydrogen) and an easily scalable process to tailor the required hydrogen and to modify the structural, electronic energy band structure of $TiO_2$ to realize the improvements in photocatalytic properties is of utmost importance.

Therefore, in this work we used 5% $H_2$ in Ar to modify optical absorption by creating defect/disordered states in the $TiO_2$ lattice and studied photocatalytic degradation of methylene blue to be used in photoelectrochemical water splitting applications. This is the new experimental approach to tailor the optical, electrical and photocatalytic properties of $TiO_2$ in a controlled way. The hydrogen treated brownish $TiO_2$ nanoparticles with long-wavelength absorption showed much better performance in photocatalytic decomposition of methylene blue and phenol than pure $TiO_2$ nanocrystals. In our hydrogen treated $TiO_2$ samples, localized $Ti^{3+}$ centres were identified, which explain the origin of the modified electronic structure. In order to further elucidate the conditions under which localized $Ti^{3+}$ states rather than delocalized shallow donor states are formed upon hydrogen treatment, *ab initio* calculations within the density functional theory (DFT) of $TiO_2$ with varying concentrations of oxygen vacancies and oxygen vacancies occupied by atomic hydrogen were performed.

## 2. Experimental procedures

### 2.1 Synthesis of $TiO_2$ nanoparticles

Pristine $TiO_2$ nanocrystals were prepared by a wet chemical method using titanium tetra-isopropoxide, ethanol, hydrochloric acid and deionized water as reported earlier.[23] In brief, 25 mL deionized water mixed with 1 mL hydrochloric acid was added slowly to 10 mL of titanium tetra-isopropoxide with continuous stirring in an ice bath. A white precipitate solution was obtained, which was filtered and heated in air at 80 °C to evaporate extra water. After evaporation of water, the white precipitate was sintered at 400 °C for 4 h. For the hydrogen treatment under partial pressure, the annealing chamber was pumped down to $2.0 \times 10^{-6}$ Torr and 20 sccm. 5% $H_2$ balanced Ar was introduced into the chamber while maintaining the chamber pressure at $2 \times 10^{-2}$ Torr. The annealing temperature was set at 300 °C for 10, 20 and 30 h followed by cooling down for 1 h.

### 2.2 Materials characterization

Glancing angle X-ray diffraction and Raman analysis were carried out on a Philip's X'Pert PRO-PW vertical system operating in reflection mode using Cu Kα ($\lambda = 0.15406$ nm) radiation and an Invia Raman microscope using a 514 nm argon ion laser pulse for excitation, respectively. To understand the optical behavior, the UV-visible spectra were measured on a Perkin-Elmer Lambda 35 UV visible spectrometer in the wavelength range of 200–800 nm. About 50 mg of $TiO_2$ nanocrystals were pressed into a small sample container to make a flat surface and uniform density in a 'Praying Mantis' diffuse reflection accessory. Fourier transform infrared spectroscopy (FTIR) analysis was performed at room temperature using a Nicolet 5700 spectrometer in transmission mode in the wavenumber range of 500–4000 $cm^{-1}$. The spectroscopic grade KBr pellets were used for collecting the spectra with a resolution of 4 $cm^{-1}$ performing 32 scans. All the measurements were conducted under ambient conditions in air. TEM (FEI-Technai-G20 with a LaB6 filament, operating at 200 keV) was used to study the size and structural properties of nanoparticles. Proton Nuclear magnetic resonance ($^1$H-NMR) measurements were carried out to investigate the effect of hydrogen treatment on $H:TiO_2$ using a Nuclear Magnetic Resonance Spectrometer (JEOL-JNM-ECA Series (Delta V4.3)-400 MHz-FT-NMR). The EPR spectra were recorded on a Bruker EPR 100d X-band spectrometer for pristine and $H:TiO_2$ samples through the EPR cavity. *G* values were calibrated using a di(phenyl)-(2,4,6-trinitrophenyl)iminoazanium (DPPH) sample. The parameters utilized in EPR measurements are as follows: center field, 3512 G; frequency, 9.74 GHz; microwave power, 20 mW. X-ray photoelectron spectroscopy (XPS, Kratos, XSAM 800) was carried out with non-monochromatic Mg ($h\nu = 1253.6$ eV) radiation. All binding energies were calibrated by referencing to the C1s peak at 284.6 eV. The deconvolution of the Ti peaks was performed through CASA XPS software.

### 2.3 Photocatalytic experiments

The photocatalytic performance of pristine and hydrogen treated $TiO_2$ samples was evaluated by observing their abilities to degrade the methylene blue (MB) dye, which is adopted as a representative organic pollutant in wastewater, in aqueous solution under simulated visible irradiation induced by using a 100 W tungsten lamp equipped with a UV cut-off filter to remove the radiation below 380 nm.

In a typical visible-light photocatalytic experiment, the catalyst (30 mg) was dispersed in a 100 mL aqueous solution of MB (10 μM) and the obtained catalyst suspensions were magnetically stirred at 250 rpm in the dark for 40 min to ensure adsorption/desorption equilibrium between the catalyst and organic dye. The catalyst suspension was subsequently irradiated with a 100 W tungsten lamp. A sufficient dye solution (2 mL) of the suspension was extracted and centrifuged after every 10 min during the course of 100 min irradiation to remove the residual catalyst particulates for analysis. Control experiments were performed either without the catalyst or in the dark to attest that the degradation reaction is solely by a photocatalytic process. The photodegradation efficiency was monitored by measuring the change in intensity of the characteristic absorbance peak of MB at 664 nm using a Shimadzu UV-2450 spectrometer with 10 mm path length quartz cells. The photodegradation efficiency ($D$) of each catalyst was determined using the following equation:

$$D(\%) = 100 \times (C_0 - C)/C_0 \tag{1}$$

here $C$ is the concentration of MB at the time interval $t$ and $C_0$ is the concentration after the adsorption equilibrium is reached before irradiation.

### 2.4 Photoelectrochemical and electrochemical impedance spectroscopy

For photoelectrochemical and electrochemical impedance spectroscopy (EIS) measurements, thin films from $TiO_2$ powders were prepared using sol–gel spin coating techniques. These measurements were carried out in a three-electrode photoelectrochemical cell using pristine and $H:TiO_2$ thin films as the working electrode, Pt as the counter electrode and Ag/AgCl as the reference electrode in a 1 M NaOH electrolyte (pH = 13.6). The photoelectrochemical cell was controlled using a CIMPS-2 (Controlled Intensity Modulated Photospectroscopy) system consisting of a Zennium Electrochemical Workstation (X-Pot Potentiostat). For photoelectrochemical measurements, linear sweep voltammetry scans under dark and illumination were carried out in the potential range of −1.0 to +1.0 V *versus* Ag/AgCl with a scan rate of 20 mV $s^{-1}$. The illumination source was a white light source ($\lambda > 380$ nm) having an output illumination intensity of 100 mW $cm^{-2}$. The electrochemical impedance spectroscopy (EIS) measurements were carried out in the frequency range from 100 kHz to 0.01 Hz with an AC signal amplitude of 10 mV under open bias conditions (*i.e.* 0.0 V *versus* Ag/AgCl reference electrode) to obtain the physical parameters such as flat band potential, carrier concentration, carrier conductivity, charge separation, and recombination processes.

### 2.5 *Ab initio* simulations

For the *ab initio* calculations we used the Vienna *ab initio* simulations package (VASP).[24] In VASP the valence electrons are described by using a plane wave basis set and the core electrons are taken into account using the projector-augmented wave formalism.[25,26] All simulations were carried out within the PBE + $U$ framework.[27] Here, the properties of the strongly correlated d-electrons are corrected by using a Hubbard-like term for the onsite Coulomb interactions. We used a value of 4 eV for the Hubbard parameter $U$ very close to the choice used in previous studies on n-type defects in $TiO_2$.[28–31] For the energy cut-off that defines the plane wave basis set we used a value of 500 eV. For modelling hydrogen treated anatase $TiO_2$ with different levels of disorder, we used 3 × 3 × 1 super cells. Reciprocal space was sampled by using a 3 × 3 × 4 grid including the $\Gamma$ point and by using a Gaussian smearing with a width of 0.1 eV. Structural relaxations were performed until all forces were smaller than 0.02 eV $Å^{-1}$. The unit cell vectors were optimized simultaneously with the ion positions until pressures smaller than 1.0 kbar (0.1 GPa) were reached. In those cases where external pressure was applied the unit cell vectors were varied until the target pressures were reached within the same accuracy of at least 1.0 kbar.

In order to calculate optical absorption coefficients we determined the frequency dependent dielectric function of the material by *ab initio* methods. The wavelength dependent absorption coefficient $\alpha(\lambda)$ is given by[32]

$$\alpha(\lambda) = \frac{2\pi}{\lambda}\sqrt{2(|\varepsilon| - \varepsilon_r)} \tag{2}$$

where $\varepsilon$ is the complex frequency dependent dielectric function and $\varepsilon_r$ is its real part.

The imaginary part $\varepsilon_i$ of the dielectric function was calculated by a summation over matrix element products between the occupied and unoccupied Kohn–Sham eigenstates using the VASP software package as described by Gajdošet *et al.*[33] The real part of the dielectric function was derived *via* the Kramers–Kronig relation. Off-diagonal elements of the dielectric function were found to be strongly suppressed and were hence ignored. An average over the diagonal elements of $\varepsilon$ was used as an input for the calculation of the absorption coefficient in order to take into account the absence of any predominant orientation in polycrystalline materials.

## 3. Results and discussion

To determine the crystal structure and possible phase changes after hydrogen treatment, X-ray diffraction (XRD) spectra were collected from the pristine and hydrogen treated $TiO_2$ nanocrystal samples at 300 °C for different times (Fig. 1(a)). All the peaks in the XRD pattern of pristine and $H:TiO_2$ exhibited feature characteristics of the tetragonal anatase $TiO_2$ crystallographic phase. Major peaks are observed at $2\theta$ angles of 25.3, 37.84, 48.07, 53.95, and 55.10° with $d_{hkl}$ of 3.51, 2.37, 1.89, 1.69, and 1.66 Å corresponding to diffraction from planes (101), (044), (200), (105) and (211), respectively. Therefore, the tetragonal anatase phase of $TiO_2$ has been retained without any

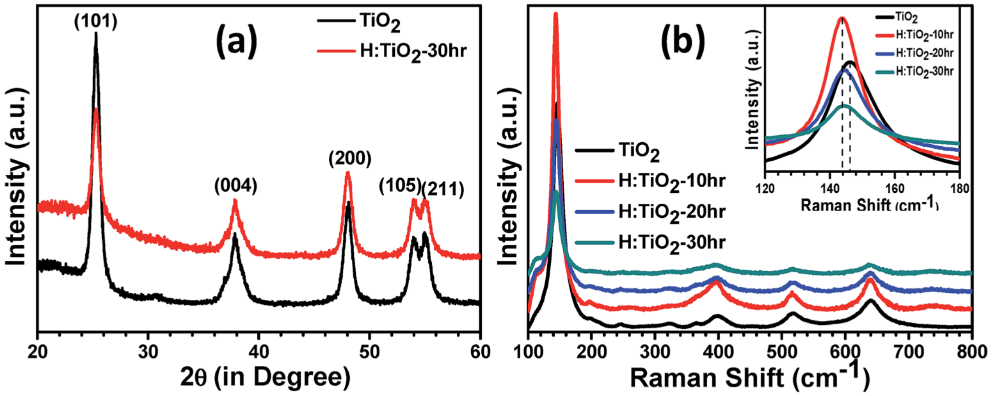

Fig. 1 (a) XRD and (b) Raman spectra of the pristine and hydrogen treated $TiO_2$ nanocrystals.

structural transformation even after hydrogen treatment at 300 °C for 30 hours. The annealing of $TiO_2$ in hydrogen ambient may affect $TiO_2$ in two ways. It can lead to the formation of $TiH_2$ (ref. 34) or the hydrogen would react with the oxygen in $TiO_2$ leading to the formation of lattice defects.[35] Since XRD data did not indicate any peak corresponding to $TiH_2$, the reduction of $TiO_2$ resulting in the formation of lattice defects such as oxygen vacancies is more likely. Both $TiO_2$ and H:$TiO_2$ samples show similar diffraction patterns (Fig. 1(a)). The slightly weaker XRD diffraction peak intensity in H:$TiO_2$ indicates that the crystallinity of H:$TiO_2$ upon hydrogen treatment is decreased due to defect generation and/or some degree of surface disorder.

To further study any change in the phase structure after hydrogen treatment, Raman spectroscopy was performed on pristine and H:$TiO_2$ as shown in Fig. 1(b). Well-resolved $TiO_2$ Raman peaks were observed at 144 $cm^{-1}$ ($B_{1g}$), 398 $cm^{-1}$ ($B_{1g}$), 515 $cm^{-1}$ ($E_g$), and 640 $cm^{-1}$ ($E_g$) in the spectra of all samples, indicating that anatase nanoparticles are the predominant species. Only the peak expected at 147 $cm^{-1}$ ($E_g$) was not visible, which may be suppressed by a much stronger $TiO_2$ peak at 144 $cm^{-1}$ ($B_{1g}$) line.[36] No major effects of hydrogen treatment with time were observed on the position of peaks in Raman spectra, *i.e.*, the anatase structure is retained after hydrogen treatment. However, peak broadening in the H:$TiO_2$ samples was observed in all the peaks in comparison to pristine. Such peak broadening in the Raman spectrum is assigned to structural changes in H:$TiO_2$ indicating the formation of oxygen vacancies and other defects in the lattice.

Fig. 2 shows the diffuse reflectance spectra (DRS) of pristine and hydrogen treated black $TiO_2$ nanocrystals. A steep increase in absorption at wavelengths shorter than 375 nm can be attributed to the intrinsic band gap of crystalline anatase $TiO_2$. H:$TiO_2$ samples with different durations of treatment show a significant shift of absorption edge towards higher wavelength sliding to visible light absorption. Especially for the H:$TiO_2$ sample treated in hydrogen for 30 h, the increase in absorption is observed in the wavelength range of 375–675 nm. The increased absorption is much higher as compared to other modification techniques used for $TiO_2$ layers. The calculated values of the band gap energy from diffusive reflectance (inset (a) of Fig. 2) show that the band gap of the pristine $TiO_2$ nanocrystals is approximately 3.30 eV, slightly higher than that of bulk anatase $TiO_2$. The onset of light absorption for the hydrogen treated brownish $TiO_2$ nanocrystals was lowered to about 2.59 eV. A digital photograph of pristine and hydrogen treated $TiO_2$ nanocrystals is shown in the inset of Fig. 2(b) and (c), clearly showing the drastic change in the optical properties upon hydrogen treatment.

In order to investigate the changes in the microstructure upon hydrogen treatment, high-resolution transmission electron microscopy (HR-TEM) studies were carried out on the pristine and hydrogen treated brown $TiO_2$ nanocrystals as shown in Fig. 3. The pristine $TiO_2$ nanocrystal is completely crystalline, displaying clearly resolved and well-defined lattice fringes, terminating quite sharply at the surface of the nanocrystals (Fig. 3(a)). However, HR-TEM images of hydrogen treated black H:$TiO_2$ nanoparticles exhibit a disordered amorphous shell layer structure around the crystalline $TiO_2$ core resulting in crystalline core/amorphous shell ($TiO_2$@H:$TiO_2$) nanostructures as shown in Fig. 3(b). The average size of individual nanoparticles is approximately 15 nm in diameter. The disordered layer on the surface of H:$TiO_2$ is ≈1–2 nm in

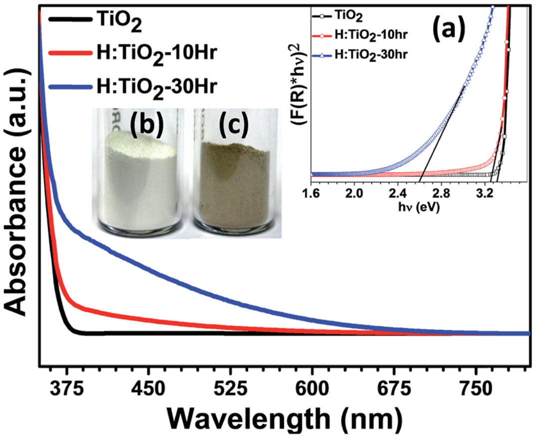

Fig. 2 Diffuse reflection spectra of pristine and hydrogen treated $TiO_2$ nanocrystals. The inset (a) shows the transformed Kubelka–Munk spectrum. (b) and (c) show the actual digital photograph of pristine and hydrogenated $TiO_2$ nanocrystals.

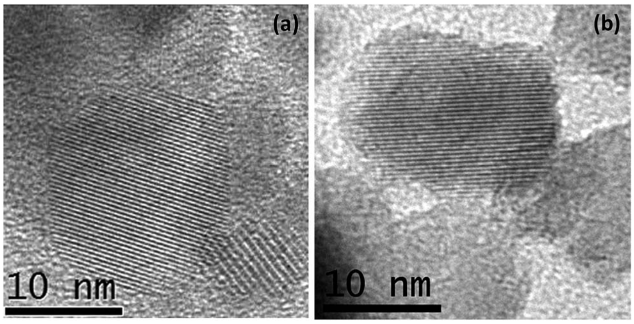

Fig. 3 HR-TEM images of (a) pristine and (b) hydrogen treated $TiO_2$ nanocrystals for 30 h.

thickness coated on a crystalline core after the hydrogen treatment for 30 h. From these values we can estimate that the fraction of the disordered material is between 15 and 25% of the total volume.

More insights into chemical changes caused by the hydrogen treatment on $TiO_2$ were obtained by Fourier transform infrared (FT-IR) spectroscopic measurements. The results are shown in Fig. 4(a). FT-IR spectra of both pristine and hydrogen treated samples show similar absorption features from 500 $cm^{-1}$ to 4000 $cm^{-1}$ and exhibit OH absorption bands near the 1635 $cm^{-1}$ and 3400 $cm^{-1}$ region. The characteristic feature of the spectrum symmetric stretching vibrations of the Ti–O bonds is the presence of a band in the region of 400–800 $cm^{-1}$ which is due to the $TiO_6$ octahedra. After hydrogen treatment, the intensity of OH absorption bands is decreased near the 3400 $cm^{-1}$ which suggests that the hydrogen treatment prevents the passivation of more O dangling bonds as this would otherwise increase the absorption. The wider OH absorption band in $H:TiO_2$ indicates that the $H:TiO_2$ surface provides the more diverse environment for the absorption of OH bands than the pristine $TiO_2$.[14]

We further examined $TiO_2$ and $H:TiO_2$ by $^1H$ NMR measurements to study the role of hydrogen treatment under partial pressure conditions. Fig. 4(b) shows the $^1H$ NMR data of pristine and $H:TiO_2$ nanocrystals with broad peaks at chemical shifts of 3.74 and 3.87 ppm, respectively. The $^1H$ NMR spectra of $H:TiO_2$ samples show a large line width which may be due to the incorporation of H at bridging sites at the disordered surface produced during the hydrogen treatment under partial pressure, or may be due to the bridging sites located on different crystallographic planes on the surface.[37,38] Additionally, pristine $TiO_2$ shows two narrow peaks at chemical shifts of +0.22 ppm and −0.77 ppm. However, the hydrogen treated $H:TiO_2$ sample shows a pronounced additional peak at a chemical shift of −1.07 ppm. This new peak at $\delta = -1.07$ ppm in $H:TiO_2$ is probably due to the presence of weakly bound hydrogen atoms as a result of the hydrogen treatment process and may provide an explanation for the enhanced hydrogen mobility in black $TiO_2$.[37] Considering the theoretical studies, we may conclude that the weakly bound hydrogen atoms are frequently absorbed by oxygen vacancies in $H:TiO_2$.[39–41]

Electron paramagnetic resonance (EPR) spectroscopy was used to determine the presence of unpaired electron spins corresponding to localized $Ti^{3+}$ centers. To provide a clear picture of the existence of $Ti^{3+}$ in hydrogen treated $H:TiO_2$, we performed the EPR measurement on $TiO_2$ treated in 5% $H_2$ mixed Ar at 300 °C for 30 hours. As shown in Fig. 5, the pristine $TiO_2$ possesses a very weak resonance signal at a $g$-value of 2.08 which results from surface adsorbed $O_2^-$ from air.[42,43] This confirms that pristine $TiO_2$ contains almost only $Ti^{4+}$ ($3d^0$) ions and exhibits weak unpaired electron signals. For the sample treated with hydrogen for 30 h, a strong EPR signal was observed with a $g$ value of 1.95, which is a characteristic of paramagnetic $Ti^{3+}$ centers.[17] The formation of $Ti^{3+}$ centers is frequently explained by the generation of oxygen vacancies during the reduction of $TiO_2$ by hydrogen treatment. The strong EPR signal in $H:TiO_2$ confirms that the vacuum hydrogen treated $TiO_2$ nanocrystal sample contains a large concentration of $Ti^{3+}$ and oxygen vacancies.

XPS measurements were carried out on both pristine and hydrogen treated $TiO_2$ nanoparticles to understand the surface chemical bonds. In order to understand the chemical composition, peak position and hence the electronic properties, the $Ti2p_{3/2}$ core level spectra were fitted with a mixture of Gaussian and Lorentzian line shapes, where Gaussian takes care of instrumental broadening and Lorentzian for the core hole life time with a Shirley background. Fig. 6(a) and (b) show a peak at

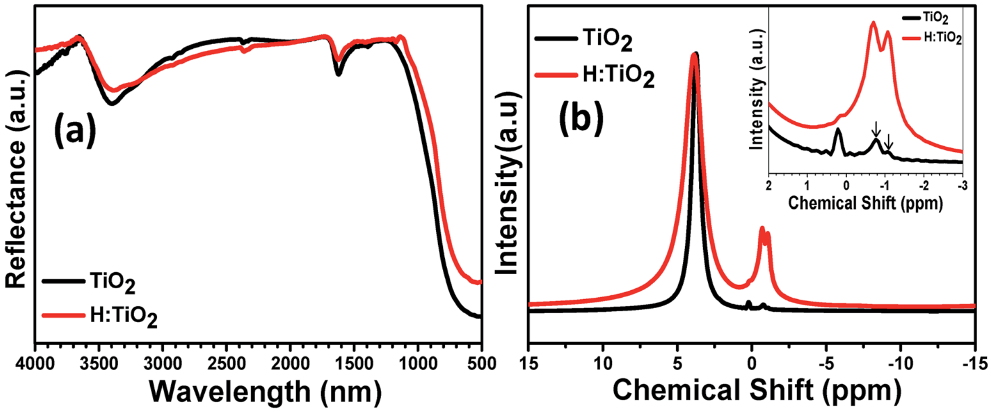

Fig. 4 (a) FTIR and (b) $^1H$ NMR spectra of the pristine and hydrogen treated $TiO_2$ nanocrystals.

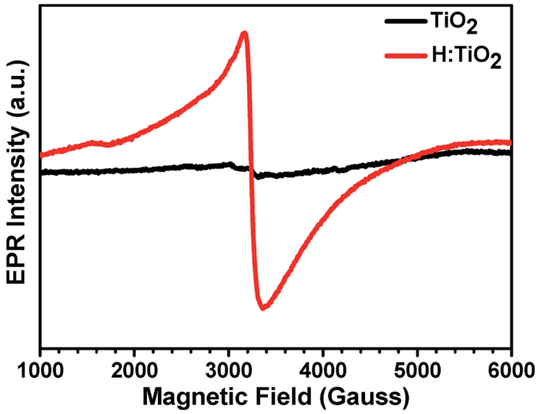

Fig. 5 EPR spectra of pristine and hydrogen treated $TiO_2$ samples recorded at 300 K. The *g* values of the H:$TiO_2$ sample indicated in the figures correspond to the minima or maxima of the different $Ti^{3+}$ EPR lines.

a binding energy of 459 ± 0.1 eV which is attributed to $Ti^{4+}$ states for both $TiO_2$ and hydrogen treated $TiO_2$.[44,45] However, for hydrogen treated $TiO_2$ a new peak is observed at a binding energy of 456.2 ± 0.1 eV which is attributed to $Ti^{3+}$ as shown in Fig. 6(b), indicating a different bonding environment which is due to hydrogen treatment that creates disorder in the lattice, resulting in the near surface $Ti^{3+}$. Fig. 6(c) and (d) represent the O1s spectra of $TiO_2$ systems. The peak at a binding energy of 530.4 ± 0.1 eV corresponds to O–Ti bonds in titanium dioxide. The second component is broader at a binding energy of 531.6 ± 0.1 due to Ti–OH bonds.[46] The reduction in the hydroxyl component could be due to the combination of desorption of hydroxyl groups and the influence of hydrogen treatment.

It has been further proposed by experimental[17] and theoretical[39–41] studies that atomic hydrogen gets preferably absorbed at the oxygen vacancies in $TiO_2$. In the work of Wang *et al.*,[17] it was concluded that all oxygen vacancies get occupied by atomic hydrogen leading to the conversion of stoichiometric $TiO_2$ to the composition $TiO_{2-x}H_x$. This finding was rationalized by the absence of any localized $Ti^{3+}$ centers which are typically formed near oxygen vacancies. This reasoning is supported by our simulations as will be discussed later on. Since we do find a strong EPR signal of localized $Ti^{3+}$ states in our samples and as the samples were synthesized under rather mild hydrogen conditions, it can be concluded that the majority of

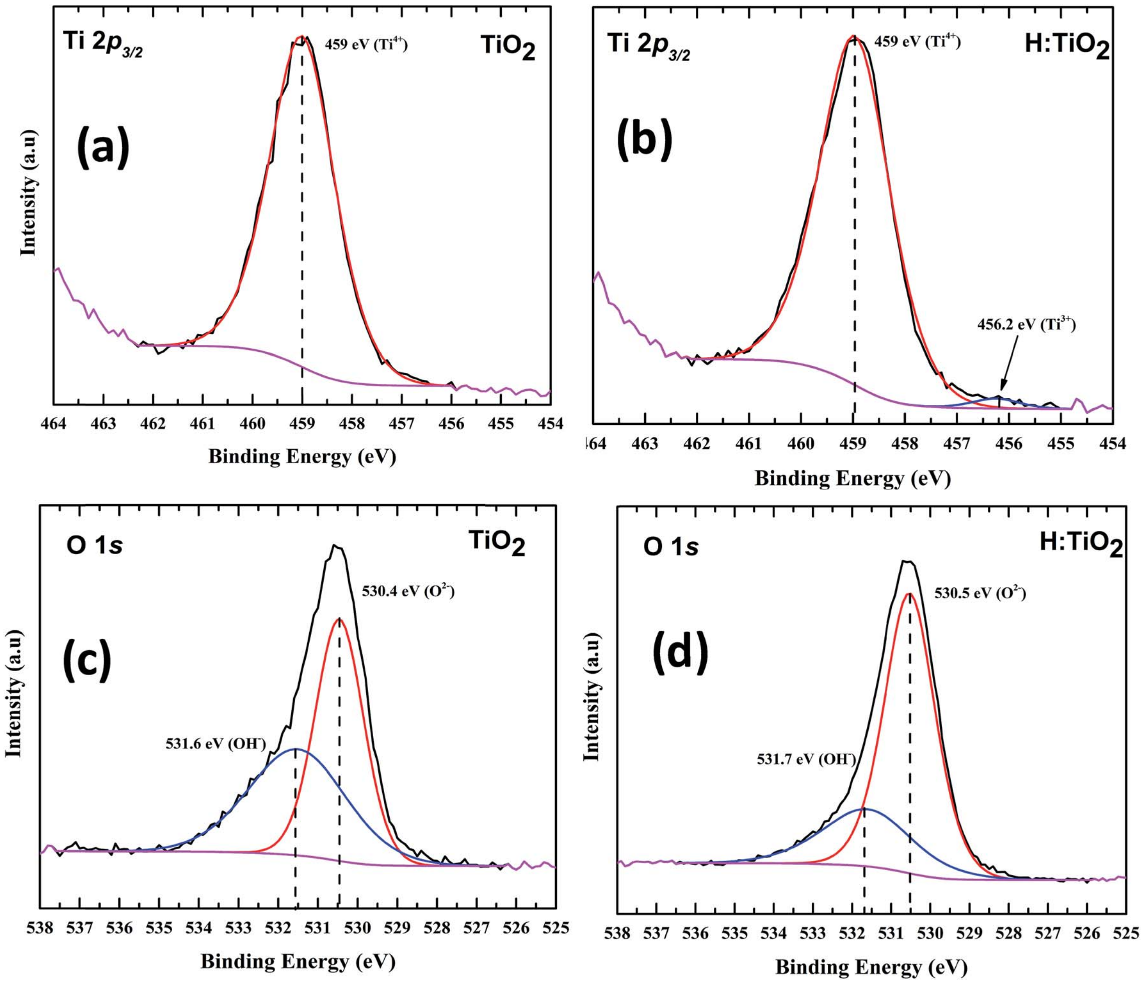

Fig. 6 XPS spectra of (a) Ti2p of pristine $TiO_2$, (b) hydrogen treated $TiO_2$ shows the presence of $Ti^{3+}$ (c) O1s of $TiO_2$ and (d) O1s of hydrogen treated $TiO_2$.

oxygen vacancies are not occupied by atomic hydrogen, at least in our case. As previous experimental studies[14,41,47] and our simulation results discussed below show, a high concentration of oxygen vacancies and $Ti^{3+}$ centers introduces occupied mid-gap states, which substantially narrow the electronic band gap of $TiO_2$. Photoexcitation of these states correspondingly leads to a narrow optical band gap in agreement with our DRS measurements (Fig. 2) and potentially to enhanced visible-light photocatalytic activity.

The experimental results clearly indicate the relevance of enhanced visible light absorption which is one of the main reasons for improving the photoelectrochemical performance of $TiO_2$. It is important to understand the crucial role of hydrogen treatment in forming localized electronic mid-gap states in the form of $Ti^{3+}$ centers as experimentally observed in this work. In different studies oxygen vacancies (pristine $V_O$ or occupied by atomic hydrogen $H_O$) have been investigated as prototypical defects associated with the reduction of $TiO_2$ by hydrogen in order to elucidate the modification of the electronic structure and optical absorption properties. In many cases,[47,48] the blackening of hydrogen treated $TiO_2$ is traced back to the formation of localized $Ti^{3+}$ states in the $TiO_2$ band gap enabling the absorption of photons from the visible light spectrum. However, hydrogen treatment of $TiO_2$ can also lead to the generation of a high density of occupied delocalized electronic states which act as shallow electron donors and hence lead to a high concentration of mobile charge carriers.[17]

In order to elucidate the conditions which favor the generation of localized or delocalized electrons after the reduction of $TiO_2$ we studied in this work the energetics of localized and delocalized states induced by different defect types, in terms of defect concentration and external pressure. We have used anatase supercells of the composition $Ti_{36}O_{72}$ which are generated by a 3 × 3 × 1 repetition of the tetragonal anatase unit cell. The dimensions of the optimized defect free supercell are $1.17 \times 1.17 \times 0.97$ nm$^3$. Different supercell compositions for oxygen vacancies $Ti_{36}O_{72-x}$ ($V_O$ defects), and hydrogen saturated oxygen vacancies $Ti_{36}O_{72-x}H_x$ ($H_O$ defects), $x = 0, 1, 6, 10$, were considered. These correspond to defect concentrations of 0, 1.4, 8.3 and 13.9% with respect to the number of oxygen atoms. The corresponding structures for the case of $V_O$ defects are shown in Fig. 7. The disorder in the material was modeled by placing the lattice defects on random sites in the super cell. The positions of the impurities were chosen such that defects on adjacent sites are avoided since these configurations are energetically disfavored.

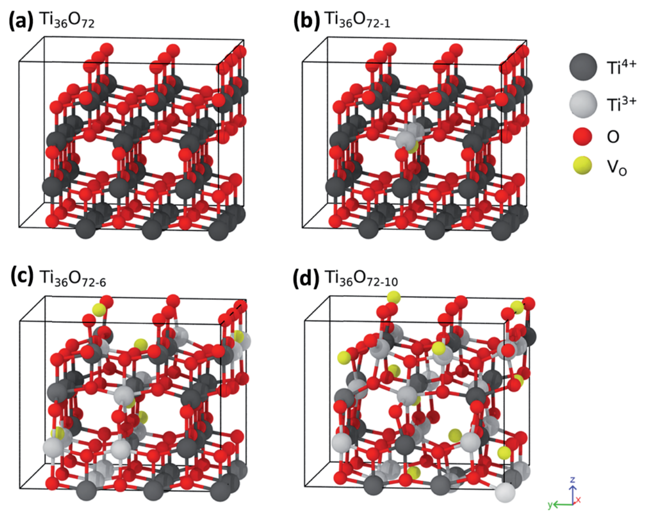

Fig. 7 (a–d) 3 × 3 × 1 supercells of $TiO_2$ containing 0, 1, 6 and 10 $V_O$ defects, respectively. The positions of the oxygen vacancies are indicated by yellow spheres, oxygen ions are shown in red and Ti ions in grey. $Ti^{3+}$ centres are shown as bright grey spheres and $Ti^{4+}$ ions as dark grey spheres.

We start the discussion of the *ab initio* calculations with the results concerning the conditions that favor or disfavor the generation of localized $Ti^{3+}$ centers or delocalized shallow donor states due to $V_O$ and $H_O$ defects. As a measure for the stability of the localized $Ti^{3+}$ states we calculated the localization energy $E_{loc} = \frac{E_{deloc} - E_{loc}}{\#(\text{defects})}$ for varying concentrations of $V_O$ and $H_O$ defects and varying external pressure. Here $E_{deloc}$ and $E_{loc}$ are the ground state energies of the defective $TiO_2$ unit cells with delocalized and localized $Ti^{3+}$ states, respectively, and #(defects) is the number of defects per unit cell. Hence, positive values of $E_{loc}$ indicate that localization is more favorable than delocalization. We find that the localized states tend to be more stable at higher defect concentrations for both defect types (Fig. 8(a)). At higher concentrations of $H_O$ and $V_O$ defects similar localization energies in the range from about 0.2 to 0.45 eV are obtained in both cases, indicating the formation of localized $Ti^{3+}$ centers. However, at the lowest considered defect concentration, corresponding to a single defect in the 3 × 3 × 1 supercell, the behavior of the two defect types deviates substantially. Here, the delocalized solution is slightly favored in the case of the $H_O$ defect by 0.03 eV, while the $V_O$ defect leads to a localized solution with $E_{loc} = 0.22$ eV. The latter value is in reasonable agreement with hybrid functional calculations[22] where $E_{loc} = 0.17$ eV was found. The formation of a delocalized solution in the case of a low concentration of $H_O$ defects is in good agreement with the experimental work of Wang *et al.*[17] who assumed that the substitution of oxygen by hydrogen leads to the observed high densities of delocalized mobile charge carriers. Selected HSE06 hybrid functional calculations confirmed the delocalized ground state of the electron donated by the $H_O$ defect at the lowest considered defect concentration of 1.4% and the full localization of the additional electrons at 8.3% defect concentration (see ESI for details†). The external isotropic pressure was considered as a further parameter that might determine the localization energy for single $V_O$ and $H_O$ defects in the 3 × 3 × 1 supercell. Here our *ab initio* calculations predict the transition from localized mid-gap states to delocalized shallow donor-states with increasing external pressure for both defect types (Fig. 8(b)). The sensitivity of the localization energy to pressure is more pronounced in the case of the $V_O$ defects. While the transition takes place at negative (expansive) pressure for the $H_O$ defects, compressive pressures larger than 5 GPa are needed to enforce delocalization in the case of $V_O$ defects. The origin of the pressure dependence of the

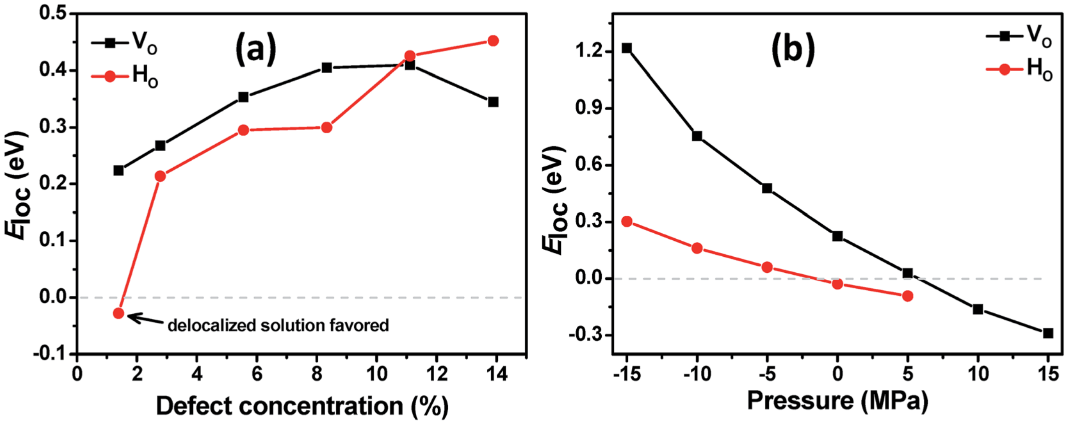

Fig. 8 Localization energy $E_{loc}$ per defect for the excess charge carriers induced by $V_O$ and $H_O$ defects as a function of (a) defect concentrations and (b) external pressure for a single defect. Positive values of $E_{loc}$ mean that the localized $Ti^{3+}$ centers are more stable than the delocalized shallow donor states. For the $H_O$ defects localized solutions could not be stabilized in the *ab initio* simulations at pressures >5 GPa.

localization energy can be traced back to the lattice distortion of the localized $Ti^{3+}$ centers which is easier to be accommodated in an expanded lattice. Structural analysis shows that the lattice distortions are locally confined near the $Ti^{3+}$ centers and can hence be considered as small polarons.[29]

In the next step the electronic structure modification of $TiO_2$ depending on the concentration of $V_O$ and $H_O$ defects is investigated. The presence of localized $Ti^{3+}$ centers can be associated with the formation of occupied mid gap states in the density of states (DoS). As shown in Fig. 9(a), at low concentrations of oxygen vacancies of about 1%, we find two mid gap states, 0.74 eV and 1.11 eV, below the conduction band minimum (CBM), which are formed by two localized $Ti^{3+}$ centers in the vicinity of the respective oxygen vacancies. These are shown in Fig. 7 as grey spheres and their effect on the density of states is in good agreement with previous *ab initio* studies on single oxygen vacancies.[30] As discussed above, at the lowest considered concentration of $H_O$ defects the delocalized solution is favored such that in this case no midgap state is present in the DoS (Fig. 9(b)). At higher defect concentrations occupied midgap states are present for both defect types and the respective midgap state spectra broaden and shift down towards the valence band maximum, although the broadening of the spectrum is considerably more pronounced for the $V_O$ defects. In order to facilitate the comparison, the DoS of the different defect concentrations in Fig. 9(a) and (b) were aligned with respect to the center of the O2s band which is only weakly affected by the presence of $V_O$ and $H_O$ defects, see ESI Fig. S2.†

We obtain qualitatively similar results employing the HSE06 hybrid functional as shown in Fig. S1 of the ESI.† Both methods predict the double peak in the midgap region for a single $V_O$ defect and the considerably broadened and down shifted spectrum of defect states at higher $V_O$ concentrations. In the case of the $H_O$ defects, in both methods no midgap state is formed at low defect concentrations while at higher defect concentrations a relatively narrow spectrum of defect states forms below the CBM. Quantitatively, the main differences between the two approaches are the deviating predictions for

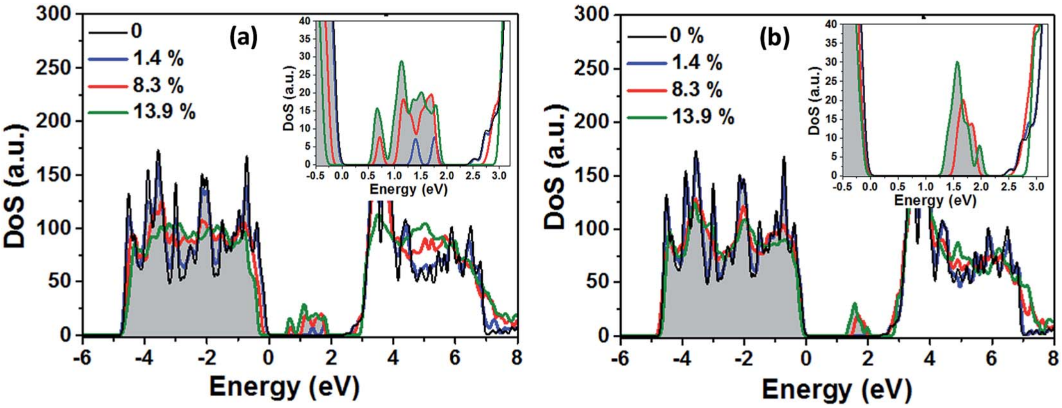

Fig. 9 Density of states (DoS) of anatase $TiO_2$ for different concentrations of oxygen vacancies $V_O$ in (a) and substitutional $H_O$ defects in (b). The band gap areas are enlarged and shown as insets. Shown are the densities of states for 0, 1, 6 and 10 defects in the 3 × 3 × 1 supercell. This corresponds to defect concentrations of 0%, 1.4%, 8.3% and 13.9% with respect to the number of oxygen atoms. The highest occupied state of pristine $TiO_2$ sets the zero energy. Occupied energy levels are indicated by the grey shading.

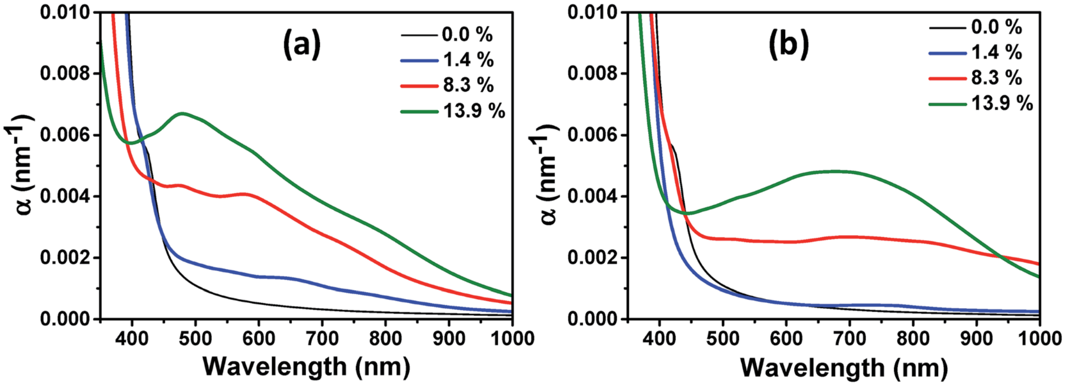

Fig. 10 Absorption coefficient $\alpha$ of anatase $TiO_2$ with different concentrations of (a) oxygen vacancies $V_O$ and (b) substitutional $H_O$ defects. A higher concentration of oxygen vacancies leads to a considerable photo-absorption in the visible spectrum. No saturation in the photo-absorption is observed up to the investigated vacancy concentrations. Note that the simulations indicate that already the defect free anatase $TiO_2$ seems to absorb visible light at the low wavelength limit. This inconsistency with the experiment is due to the underestimation of the electronic band gap by the employed PBE + *U* method which leads to a red-shift in the absorption spectrum.

the electronic band gap of pristine $TiO_2$ of 2.55 eV (PBE + *U*) and 3.77 eV (HSE06). Hence the PBE + *U* formalism underestimates, while the HSE06 functional overestimates the experimental value of ~3.4 eV.[22]

Finally, we investigated the effect of $V_O$ and $H_O$ defects on the optical absorption below the absorption edge of pristine $TiO_2$ and the influence of the defect concentration. In Fig. 10(a), we show the wavelength dependent optical absorption coefficient for the $V_O$ defects. Already at a low defect concentration of 1.4%, the absorption of photons with energies below the band gap energy of pristine $TiO_2$ is observed. With increasing defect concentration the absorption increases further and up to the investigated defect concentration of 13.9%, no saturation in the visible light absorption coefficient is seen, indicating that the degree of disorder is the crucial quantity that leads to the experimentally observed high photoabsorption. Consistent with the experimentally obtained DRS measurements a declining photoabsorption with increasing wavelength is observed. We note, however, that the simulated values are red-shifted with respect to the experimental data due to the underestimation of the electronic band gap. The photoabsorption spectrum of different $H_O$ defect concentrations is shown in Fig. 10(b). Here, no considerable photoabsorption in the band gap region of pristine $TiO_2$ is observed at a low defect concentration of 1.4% in accordance with the absence of a localized midgap state. At the higher defect concentrations photoabsorption in the visible light range sets in and again an increasing defect concentration leads to higher absorption coefficients. In contrast to the $V_O$ defects and the experimental data the absorption coefficient decays much slower with increasing wavelength. This suggests that the hydrogen treated samples considered in this work mainly contain oxygen vacancies. This does not exclude their partial occupancy by substitutional hydrogen.

### 3.1 Photocatalytic and photoelectrochemical activity

The photocatalytic activity of all four samples was evaluated by measuring the time-dependent degradation of methylene blue (MB) under visible-light irradiation (Fig. 11(a)). From Fig. 11(b), we can see that the pristine $TiO_2$ sample shows poor photocatalytic activity in the visible-light. The degradation rate

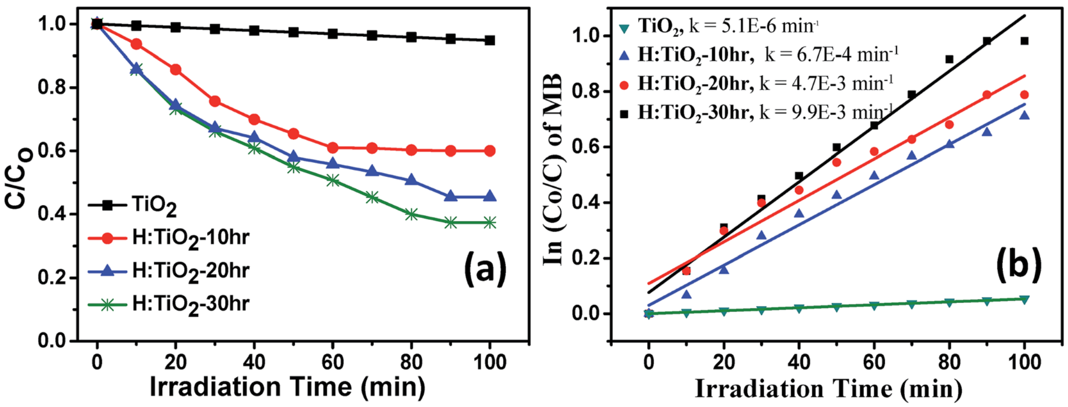

Fig. 11 (a) Solar-light driven photocatalytic decomposition of Methylene blue (b) rate constant calculation for pristine and hydrogen treated $TiO_2$ samples.

constant *k* of pristine $TiO_2$ was $\sim 5.1 \times 10^{-6}$ min$^{-1}$. This small value is attributed to the large band gap energy of $TiO_2$. For the H:$TiO_2$ samples, the photodegradation activity increases with increasing the hydrogen treatment time as expected from the enhanced visible light absorption. The photodegradation rate constant *k* reaches the maximum $\sim 9.9 \times 10^{-3}$ min$^{-1}$ for the 30 h hydrogen treated sample. This value is approximately three orders of magnitude higher than that of pristine $TiO_2$ under visible-light irradiation. Further, we have also investigated the photocatalytic degradation efficiency of pure and hydrogen treated $TiO_2$ for colorless pollutants such as phenol. The phenol degradation efficiency with different photocatalysts as a function of visible light irradiation time is given in ESI Fig. S3.† To check the long stability of the defect generated in H:$TiO_2$ by hydrogen treatment when stored under ambient conditions, we used H:$TiO_2$ samples to re-examine the structural, optical and electrical properties and also used them for photocatalytic and photoelectrochemical application tests. We found that H:$TiO_2$ samples still exhibit the presence of $Ti^{3+}$ and the enhanced photocatalytic activity for phenol degradation (Fig. S3 of the ESI†).

To determine the photoelectrochemical activity for solar hydrogen production through water splitting, thin films of pristine $TiO_2$ and H:$TiO_2$ powders were prepared using the spin coating technique on ITO substrates and converted into electrodes. The photoelectrochemical measurements were performed under visible light illumination ($\lambda = 380$ nm) with an output intensity of 100 mW cm$^{-2}$ through a tungsten lamp. The enhanced visible light photoactivity of H:$TiO_2$ was examined by measuring the linear sweep voltammetry scans under dark and illumination in the potential range of −0.5 to +1.0 V *vs.* Ag/AgCl with a scan rate of 20 mV s$^{-1}$. Fig. 12(a) shows the photocurrent density *vs.* applied potential (V *vs.* Ag/AgCl) curves for pristine and hydrogen treated $TiO_2$ samples collected in 1 M NaOH solution. In the case of pristine $TiO_2$ a very small photocurrent was obtained which is ~35 μA cm$^{-2}$ (at 1.0 V *vs.* Ag/AgCl). However, the H:$TiO_2$ samples show a large improvement in the photocurrent density (~0.56 mA cm$^{-2}$ at 1.0 V *vs.* Ag/AgCl) under the same experimental conditions.

To determine the intrinsic electrical properties of pristine $TiO_2$ and H:$TiO_2$ samples, thin films of $TiO_2$ were used as working electrodes for the Mott–Schottky ($1/C^2$ *versus* $V_{app}$) measurements. Mott–Schottky measurements were carried out at 1 kHz AC signal frequency in 1 M NaOH solution under dark conditions to calculate the donor density ($N_D$) and flat band potential ($V_{FB}$) by using the Mott–Schottky equation.[4] Fig. 12(b) shows the Mott–Schottky plots for pristine and hydrogen treated $TiO_2$ samples. The positive slope of Mott–Schottky curves in all the samples indicated the n-type conductivity of the $TiO_2$ thin films. The donor density was estimated from the slopes of the Mott–Schottky curve using the equation, $N_D = \frac{2}{\varepsilon\varepsilon_0 q}\left[\frac{d(1/C^2)}{dV}\right]^{-1}$. The calculated value of $N_{D,}$ as estimated from the slopes of the Mott–Schottky curve, was found to increase with hydrogen incorporation. The hydrogen treated H:$TiO_2$ films exhibited significantly higher donor density, $5.5 \times 10^{17}$ cm$^{-3}$, compared to the pristine $TiO_2$ ($7.2 \times 10^{16}$ cm$^{-3}$) sample even though the phase structure of the material did not show any major changes. The enhanced donor density can be attributed to excess electrons provided by lattice defects such as oxygen vacancies ($V_O$) or oxygen vacancies that are occupied by atomic hydrogen ($H_O$). Our simulation shows that delocalized excess charge carriers are rather formed by the $H_O$ defects at low defect concentrations. Since HR-TEM data show a highly defective surface of the H:$TiO_2$ samples, delocalized charge carriers can rather be expected in the bulk region of the nanocrystals, where the defect concentration should be considerably lower. The observed negative shift of flat band potential could be due to the substantially increased electron density, which is expected to shift the Fermi level of $TiO_2$ towards the conduction band.

Further, electrochemical impedance spectroscopic (EIS) measurements have been performed under visible light illumination to understand the effect of hydrogen treatment of $TiO_2$ on charge separation and recombination processes. EIS Nyquist plots of the pristine and H:$TiO_2$ samples are shown in Fig. 13. The EIS results show that only one semicircle was observed for each sample and thus can be fitted with the

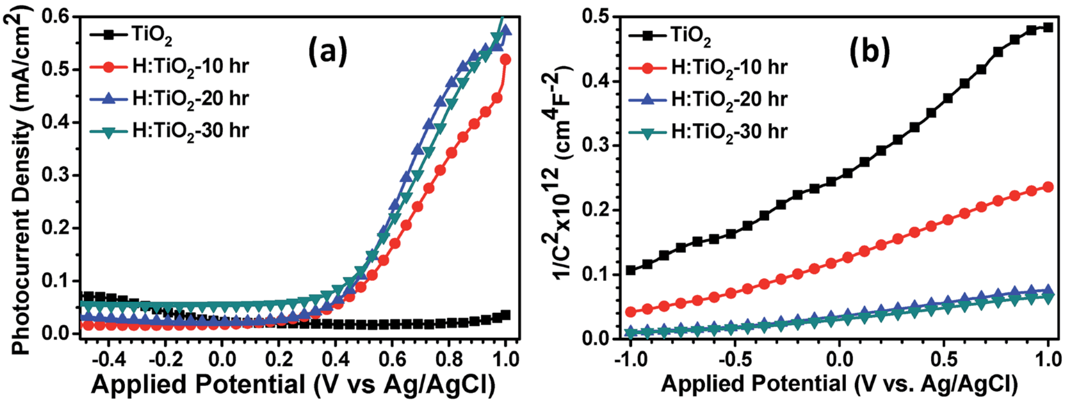

Fig. 12 (a) Photocurrent density *vs.* applied potential (V *vs.* Ag/AgCl) curves (b) Mott–Schottky plots for pristine and hydrogen treated $TiO_2$ samples collected in 1 M NaOH solution.

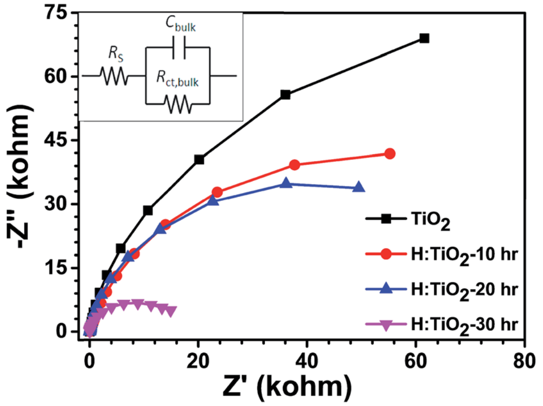

Fig. 13 EIS Nyquist plots of the pristine and hydrogen treated $TiO_2$ samples at an open bias condition under dark.

Randles equivalent circuit model (inset of Fig. 13)[49]. In this model, the element $R_S$ is the resistance related to charge transport and contains the resistance of the semiconductor catalyst, ITO substrate, the electrolyte and wire connections in the whole circuit. The elements of $R_{ct,bulk}$ and $C_{bulk}$ are related to the charge transfer at the interface of the photoelectrode/electrolyte. A smaller radius of the semicircle represents a better charge transfer ability (*i.e.*, faster surface reaction kinetics).[49] As shown in Fig. 13, it is evident that the radii of semicircle on the real axis of Nyquist plots of H:$TiO_2$ treated in hydrogen for 30 h are much smaller than those for pristine and other $TiO_2$ samples, which indicates that the hydrogen treatment in $TiO_2$ reduces the semiconductor–electrolyte contact resistance and improves the charge transport. Therefore, the charge transport efficiency of H:$TiO_2$ samples increased significantly both on the surface (*i.e.*, surface reaction kinetics) and in the bulk, leading to an improved PEC activity. The smaller radii of the H:$TiO_2$ samples are presumably due to an increased electron density as obtained in the Mott–Schottky measurement which improves the electrical conductivity of the electrodes. The smaller arc radii in H:$TiO_2$ under illumination in EIS plots clearly indicate that the fast charge transfer occurs on the photoelectrodes.

Therefore, the significant improvement in the photocatalytic activity and photocurrent density after hydrogen treatment of $TiO_2$ nanocrystals shows that they can generate more electron–hole pairs in visible light and exhibit a stronger ability for electron–hole pair separation than pristine $TiO_2$. The observation of a small photocurrent in pristine $TiO_2$ using visible light illumination ($\lambda > 380$ nm) is due to the high band gap energy as the photons with energies less than the band gap energy ($E_g = 3.31$ eV) did not contribute to the excitation of valence band electrons to the conduction band to generate the electron–hole pairs. The DRS, EPR and Mott–Schottky measurements and DFT calculation clearly show that the reduction in the band gap of H:$TiO_2$ is likely due to the formation of midgap states induced by localized $Ti^{3+}$ states. Therefore, the significant improvement in photocatalytic activity and photocurrent density can be explained by the surface disordering and defect formation after hydrogen treatment.

# 4. Conclusion

In summary, it has been shown that hydrogen treatment of $TiO_2$ under partial pressure conditions leads to an enhanced photocatalytic and photoelectrochemical response, which significantly depends on the duration of hydrogen treatment. DRS and EPR analyses of pristine and hydrogen treated $TiO_2$ nanocrystals show that the tailoring in properties of H:$TiO_2$ is due to surface oxygen-vacancies and $Ti^{3+}$ states. Additionally, these modifications in properties induced a higher charge carrier concentration and a more negative flat band potential as compared to pristine $TiO_2$. The experimental studies were substantiated by *ab initio* calculations in order to gain a deeper understanding of the origin of enhanced visible light absorption due to $Ti^{3+}$ centers and the conditions that favor the formation of localized or delocalized excess electrons due to oxygen vacancies. It was shown that with higher concentrations of $V_O$ and $H_O$ defects the spectrum of the induced midgap states broadens considerably and moves energetically downward towards the VBM. At the same time the visible light absorption increases and localization of the $Ti^{3+}$ states becomes more favorable. Substitutional $H_O$ defects at low concentrations were identified as candidates to provide delocalized charge carriers in $TiO_2$. This study provides a detailed overall picture covering experimental and theoretical aspects of the effect of hydrogen treatment on the structural, optical and electronic properties of the $TiO_2$ matrix and resulting improvements in the photoelectrochemical properties.

# Author contributions

A. P. Singh and S. Basu conceived the idea, designed the experiments and worked out the overall structure of the manuscript. M. Mehta and N. Kodan prepared and characterized the samples and analyzed the data for the experimental part of the manuscript. S. Kumar performed the catalytic measurements and was involved in writing the particular section of the manuscript. A. Kaushal performed the HRTEM and analyzed the data. A. Dey and S. Krishnamurthy performed the XPS measurements and the XPS peak fitting and were involved in writing the particular section of the manuscript. L. Mayrhofer performed and analyzed the DFT calculations and was involved in writing the manuscript. M. Walter was involved in writing the revision of the manuscript and in discussing the DFT results. M. Moseler gave advice on the setup and analysis of the DFT calculations and was involved in the interpretation and discussion of the DFT results. The manuscript was written through contributions of all authors. All authors have given approval to the final version of the manuscript.

# Acknowledgements

We gratefully acknowledge the financial support provided by the Department of Science and Technology, New Delhi India under the SERI and DST-UKERI programme and the New Indigo project InSOL. A. P. S. is grateful to the Department of Science & Technology, New Delhi, India for financial support in terms of INSPIRE Faculty award No. IFA12-PH-16. L. M. and M. M. kindly acknowledge the financial support under the FP7 project

"SOLAROGENIX" (NMP4-SL-2012-310333). The *ab initio* calculations were performed on the Joe cluster of Fraunhofer IWM and on JUROPAat the Julich Supercomputing Center (JSC). The authors gratefully acknowledge the computing time granted by the John von Neumann Institute for Computing (NIC) and provided on the supercomputer JUROPA at JSC.

## References

1 A. Fujishima, T. N. Rao and D. A. Tryk, *J. Photochem. Photobiol., C*, 2000, **1**, 1–21.

2 A. P. Singh, S. Kumari, R. Shrivastav, S. Dass and V. R. Satsangi, *Int. J. Hydrogen Energy*, 2008, **33**, 5363–5368.

3 M. R. Hoffmann, S. T. Martin, W. Choi and D. W. Bahnemann, *Chem. Rev.*, 1995, **95**, 69–96.

4 R. Dholam, N. Patel, M. Adami and A. Miotello, *Int. J. Hydrogen Energy*, 2009, **34**, 5337–5346.

5 H. Zhu, J. Tao and X. Dong, *J. Phys. Chem. C*, 2010, **114**, 2873–2879.

6 R. Asahi, T. Morikawa, T. Ohwaki, K. Aoki and Y. Taga, *Science*, 2001, **293**, 269–271.

7 S. U. M. Khan, M. Al-Shahry and W. B. Ingler Jr, *Science*, 2002, **297**, 2243–2245.

8 V. Tiwari, J. Jiang, V. Sethi and P. Biswas, *Appl. Catal., A*, 2008, **345**, 241–246.

9 P. V. Kamat, M. Flumiani and A. Dawson, *Colloids Surf., A*, 2002, **202**, 269–279.

10 A. A. Nada, M. H. Barakat, H. A. Hamed, N. R. Mohamed and T. N. Veziroglu, *Int. J. Hydrogen Energy*, 2005, **30**, 687–691.

11 M. Takeuchi, H. Yamashita, M. Matsuoka, M. Anpo, T. Hirao, N. Itoh and N. Iwamoto, *Catal. Lett.*, 2000, **67**, 135–137.

12 F. Zuo, L. Wang, T. Wu, Z. Zhang, D. Borchardt and P. Feng, *J. Am. Chem. Soc.*, 2010, **132**, 11856–11857.

13 X. Chen, L. Liu, P. Y. Yu and S. S. Mao, *Science*, 2011, **331**, 746–750.

14 X. Chen, L. Liu, Z. Liu, M. A. Marcus, W. C. Wang, N. A. Oyler, M. E. Grass, B. Mao, P.-A. Glans, P. Y. Yu, J. Guo and S. S. Mao, *Sci. Rep.*, 2013, **3**, 1510.

15 H. Li, Z. Chen, C. K. Tsang, Z. Li, X. Ran, C. Lee, B. Nie, L. Zheng, T. Hung, J. Lu, B. Pan and Y. Y. Li, *J. Mater. Chem. A*, 2014, **2**, 229–236.

16 L. X. Zheng, H. Cheng, F. X. Liang, S. W. Shu, C. K. Tsang, H. Li, S. T. Lee and Y. Y. Li, *J. Phys. Chem. C*, 2012, **116**, 5509–5515.

17 Z. Wang, C. Yang, T. Lin, H. Yin, P. Chen, D. Wan, F. Xu, F. Huang, J. Lin, X. Xie and M. Jiang, *Adv. Funct. Mater.*, 2013, **23**, 5444–5450.

18 A. Mettenborger, T. Singh, A. P. Singh, T. T. Jarvi, M. Moseler, M. Valldor and S. Mathur, *Int. J. Hydrogen Energy*, 2014, **39**, 4828–4835.

19 H. Wu, C. Xu, J. Xu, L. Lu, Z. Fan, X. Chen, Y. Song and D. Li, *Nanotechnology*, 2013, **24**, 455401.

20 A. Sasinsk, T. Singh, S. Wang, S. Mathur and R. Kraehnert, *J. Vac. Sci. Technol., A*, 2015, **33**, 01A152.

21 A. Fujishima, X. T. Zhang and D. A. Tryk, *Surf. Sci. Rep.*, 2008, **63**, 515–582.

22 C. D. Valentin, G. Pacchioni and A. Selloni, *J. Phys. Chem. C*, 2009, **113**, 20543–20552.

23 A. P. Singh, S. Kumari, Sonal, R. Shrivastav, S. Dass and V. R. Satsang, *J. Sci. Conf. Proc.*, 2009, **1**, 82–85.

24 G. Kresse and J. Furthmüller, *Phys. Rev. B: Condens. Matter Mater. Phys.*, 1996, **54**, 11169–11186.

25 G. Kresse and D. Joubert, *Phys. Rev. B: Condens. Matter Mater. Phys.*, 1999, **59**, 1758–1775.

26 P. E. Blöchl, *Phys. Rev. B: Condens. Matter Mater. Phys.*, 1994, **50**, 17953–17979.

27 S. L. Dudarev, G. A. Botton, S. Y. Savrasov, C. J. Humphreys and A. P. Sutton, *Phys. Rev. B: Condens. Matter Mater. Phys.*, 1998, **57**, 1505–1509.

28 B. J. Morgan and G. W. Watson, *Surf. Sci.*, 2007, **601**, 5034–5041.

29 B. J. Morgan, D. O. Scanlon and G. W. Watson, *J. Mater. Chem.*, 2009, **19**, 5175–5178.

30 E. Finazzi, C. D. Valentin, G. Pacchioni and A. Selloni, *J. Chem. Phys.*, 2008, **129**, 154113.

31 M. Setvin, C. Franchini, X. Hao, M. Schmid, A. Janotti, M. Kaltak, C. G. Van de Walle, G. Kresse and U. Diebold, *Phys. Rev. Lett.*, 2014, **113**, 086402.

32 M. Fox, *Optical Properties of Solids*, Oxford University Press, 2001.

33 M. Gajdošet, K. Hummer, G. Kresse, J. Furthmuller and F. Bechstedt, *Phys. Rev. B: Condens. Matter Mater. Phys.*, 2006, **73**, 045112.

34 K. M. Mackay, *Hydrogen Compounds of the Metallic Elements*, E and F N Spon, London, UK, 1966, p. 71.

35 P. Raghunath, W. F. Huang and M. C. Lin, *J. Chem. Phys.*, 2013, **138**, 154705.

36 M. Ocana, J. V. Garcia-Ramos and C. J. Serna, *J. Am. Ceram. Soc.*, 1992, **75**, 2010–2016.

37 M. Crocker, R. H. M. Herold, A. E. Wilson, M. Mackay, C. A. Emeis and A. M. Hoogendoorn, *J. Chem. Soc., Faraday Trans.*, 1996, **92**, 2791–2798.

38 P. Jonsen, *Colloids Surf.*, 1989, **36**, 127–132.

39 H. H. Nahm and C. H. Park, *J. Korean Phys. Soc.*, 2010, **56**, 485–489.

40 F. Filippone, G. Mattioli, P. Alippi and A. Amore Bonapasta, *Phys. Rev. B: Condens. Matter Mater. Phys.*, 2009, **80**, 245203.

41 U. Aschauer and A. Selloni, *Phys. Chem. Chem. Phys.*, 2012, **14**, 16595.

42 S. M. Prokes, J. L. Gole, X. Chen, C. Burda and W. E. Carlos, *Adv. Funct. Mater.*, 2005, **15**, 161–167.

43 J. Strunk, W. C. Vining and A. T. Bell, *J. Phys. Chem. C*, 2010, **114**, 16937–16945.

44 I. Luciu, R. Bartali and N. Laidani, *J. Phys. D: Appl. Phys.*, 2012, **45**, 345302.

45 U. Diebold, *Surf. Sci. Rep.*, 2003, **48**, 53–229.

46 G. Wang, H. Wang, Y. Ling, Y. Tang, X. Yang, R. C. Fitzmorris, C. Wang, J. Z. Zhang and Y. Lim, *Nano Lett.*, 2011, **11**, 3026–3033.

47 X. Liu, H. Xu, L. R. Grabstanowicz, S. Gao, Z. Lou, W. Wang, B. Huang, Y. Dai and T. Xu, *Catal. Today*, 2014, **225**, 80–89.

48 A. Naldoni, M. Allieta, S. Santangelo, M. Marelli and F. Fabbri, *J. Am. Chem. Soc.*, 2012, **134**, 7600–7603.

49 B. Klahr, S. Gimenez, F. Fabregat-Santiago, T. Hamann and J. Bisquert, *J. Am. Chem. Soc.*, 2012, **134**, 4294.